Nonlinear Dyn (2022) 108:1197–1215
https://doi.org/10.1007/s11071-022-07274-0

ORIGINAL PAPER

Hopf–Hopf bifurcation analysis based on resonance and non-resonance in a simplified railway wheelset model

Peng Guo · Caihong Huang · Jing Zeng · Hongjun Cao

Received: 23 August 2021 / Accepted: 30 January 2022 / Published online: 9 February 2022

Abstract This paper mainly investigates the dynamics of the non-resonant and near-resonant Hopf–Hopf bifurcations caused by the interaction of the lateral and yaw motion in a simplified railway wheelset model, which involves local and global dynamical scenarios, respectively. This study aims to clarify the resonances due to the wheelset instability. Firstly, the ratio of longitudinal suspension stiffness and the square of natural frequency in yawing direction denoted as the parameter k_{22} has an important impact on the transitions of distinct Hopf–Hopf bifurcations, and the ratio of the oscillation frequencies ω_1/ω_2 at the Hopf–Hopf singularity point will reduce with the decrease in k_{22} within a certain range. Secondly, the absence of strong resonance under the non-resonant condition indicates that the operation wheelset will not produce the maximum oscillation amplitude triggered by the resonance point, and several torus solutions arisen from the wheelset are obtained by numerical simulation. Thirdly, five near-resonant Hopf–Hopf bifurcations reveal that the global dynamical scenario becomes much more complex than other cases as k_{22} decreases. In particular, near the 1:4 resonant Hopf–Hopf interaction occurs when ω_1/ω_2 is close to 1:4, which has the most marked effect on wheelset hunting motions and resonances. Finally, the cyclic bifurcation behaviors under the near-resonant conditions indicate the coexistence of multiple limit cycles, and the loop of equilibria and limit cycles detected between two Hopf bifurcation points reveals that the wheelset will perform a cyclical motion in lateral and yaw direction. These results show that the change in frequency ratio induced by the intersection of the lateral and yaw motion of the unbalanced wheelset will greatly affect the hunting motions and resonances of railway vehicles. Therefore, appropriately increasing the value of k_{22} is helpful to maintain the vehicle stability.

Keywords Hopf–Hopf bifurcation · Codimension-two bifurcation · Hunting motion · Resonance · Wheelset

P. Guo · H. J. Cao (✉)
Department of Mathematics, School of Science, Beijing Jiaotong University, Beijing 100044, People's Republic of China
e-mail: hjcao@bjtu.edu.cn

P. Guo
e-mail: 20121560@bjtu.edu.cn

C. H. Huang · J. Zeng
State Key Laboratory of Traction Power, Southwest Jiaotong University, Chengdu 610031, People's Republic of China

1 Introduction

The single wheelset is an indispensable component in the process of railway vehicle regular operation. Due to nonconservative contact force, the interaction of the wheelset and track tread is accompanied by the resonance of a flutter-type self-excited oscillation when the vehicle experiences a hunting motion [9]. As a result of the complex vibration surrounding of a railway vehicle, in addition to vertical line vibration, there are longitudinal, lateral, pitch, roll, and yaw angular vibrations, which are all factors that affect the passenger amenity as well as the safety and stability of operation. Resonance is a common phenomenon in railway vehicles, which is characterized by the lowest natural frequency of the carbody in the frequency range of hunting motions [5]. There are some interactions between the wheelset and the primary suspension, the primary suspension and bogie frame, as well as the bogie frame and motor, which enable vibration to be transmitted among them. When the operating speed exceeds some critical value, or the vehicle changes track or departures and arrivals, the oscillations following a disturbance grow and eventually result in a limit cycle oscillation, which increase the risk of the hunting motions and resonances of railway vehicles.

It is found that two pairs of pure imaginary eigenvalues at $\pm i\omega_1$ and $\pm i\omega_2$ will emerge in a four-dimensional wheelset system under the certain parameters, the frequencies of lateral and yaw motion of the wheelset intersect to form a specific ratio ω_1/ω_2, which will produce rich dynamics accompanied by the superposition of multiple resonances. The strong resonance arises on the Neimark–Sacker bifurcation born at the Hopf–Hopf singularity point, hence the resonances induced by the interaction between the self-excited oscillation modes can be interpreted in the framework of the Hopf–Hopf bifurcation [1,2].

Supercritical and subcritical Hopf bifurcation phenomena were found to exist in two types of China high-speed vehicle systems [3]. These factors affecting the optimal fixed frequency of the bogie motor suspension system were investigated in [4], such as the primary and secondary suspension as well as the wheel-rail contact conditions, it was shown that proper design with the natural frequency of the traction motor far away from the frequency of the kinematic bogie oscillation is attractive to refrain motor resonance. In [5], since the unstable frequency of the bogie frame hunting motion can be controlled far lower than the frequency of the flexible carbody, the method of suspending a dynamic vibration absorber on the bogie frame to change its unstable frequency can prevent the bogie from riding at the resonant frequency of the flexible carbody and ensure that the carbody elastic vibration can be effectively controlled.

Owing to some common properties among oscillation simulators, the clear ideas and effective methods provided by a simple four-dimensional circuit model motivate us to investigate the simplified wheelset dynamic system. Revel et al. [6] explored a simple electric oscillation simulator, the main structure of the Hopf–Hopf bifurcation near 1:2 resonance is that the 1:1 and 1:2 strong resonance points emerging on two Neimark–Sacker bifurcation branches are connected by several lower-codimension singularity points. In [7], the local and global dynamics near the 2:3 resonant Hopf–Hopf bifurcation triggered by the interaction between the electric oscillation models were discussed. Several truncated normal forms including “simple” and “difficult” cases of the non-resonant Hopf–Hopf bifurcation were investigated in a coupled circuit [8], the presence of different frequency components for the quasi-periodic solutions of the two-dimensional (2D) torus and the three-dimensional (3D) torus was confirmed.

When a four-dimensional original system is converted to a truncated amplitude system, the corresponding relation between the equilibria was discussed in [1]. Among them, a trivial equilibrium e_0 with $r_1 = r_2 = 0$ of the truncated amplitude system corresponds to the equilibrium at the origin of the original system. Possible equilibria in the changeless coordinate axes of the truncated amplitude system with $r_1 = 0$ or $r_2 = 0$, called e_1 and e_2, respectively, correspond to limit cycles of the original system. Moreover, a nontrivial equilibrium e_3 with $r_{1,2} > 0$ of the truncated amplitude system yields a 2D torus of the original system. Finally, if a limit cycle is present in the truncated amplitude system, then the original system has a 3D torus.

The 1/10 scale vehicle model proposed in Yabuno et al. [9] is for theoretical and experimental research, the details of the wheelset model for the contact conditions and of the experimental derivation for the correlative parameters were shown in [9]. The nonlinear characteristics of the bifurcation based on critical velocity and the influence of the lateral linear stiffness on the nonlinear stability against disturbance were clarified in [10]. The modified wheelset model based on equivalent conicity date was investigated in [11], which showed that the feasible coexistence of stable and unstable limit cycles induced by the cyclic fold bifurcation was accompanied by the hunting motions. Two-parameter bifurcation based on two distinct nonlinear coefficients in a simplified wheelset model was explored in [12], which indicated that the variety of nonlinear coefficient can lead to a global bifurcation phenomenon. In addition, the number of turns of the periodic orbit near the strong resonance point corresponds to the resonance ratio. However, there are still several unsolved issues, for example, the global dynamics scenarios related to the resonances have not been taken into account in the wheelset model.

There are two ways for us to study the Hopf–Hopf bifurcation in a three-parameter space, one is to determine a pair of continuity parameter values d_{11} and k_{11} of the near-resonance Hopf–Hopf bifurcation based on the relationship between two frequency ratio and the third parameter k_{22}, and the other is to constantly vary the third parameter value to hunt for a pair of continuity parameter values when the near-resonance Hopf–Hopf bifurcation emerges.

In this paper, the focus is centered on Hopf–Hopf bifurcation scenarios of the simplified wheelset model to provide distinct numerical insights resulted from changes in oscillation frequency ratio. Firstly, the parameter k_{22} is of great significance to the transitions of distinct Hopf–Hopf interactions, and the result shows that the ratio of the oscillation frequencies ω_1/ω_2 at the Hopf–Hopf singularity point will reduce with the decrease in k_{22} within a certain range. Secondly, under the non-resonant condition, the absence of strong resonance on the two Neimark–Sacker branches indicates that the running wheelset will not produce the maximum oscillation amplitude induced by the resonance point. The torus solutions including unstable 2D torus, stable 3D torus and stable 2D torus emanated from the wheelset are obtained by numerical simulation. Thirdly, five global bifurcation phenomena such as near the 1:1, 2:3, 1:2, 1:3 and 1:4 resonant Hopf–Hopf bifurcations show that the dynamical scenario becomes more complex as k_{22} decreases. In particular, the case near 1:4 resonance has the most prominent influence on wheelset hunting motions and resonances. At last, under the near-resonant conditions, the cyclic bifurcation structures reveal the coexistence of multiple limit cycles arisen from the wheelset. It is worth noting that the loop of equilibria and limit cycles detected between two Hopf bifurcation points indicates that the wheelset will develop a cyclical motion in lateral and yaw direction.

The paper is organized as follows. In Sect. 2, a simplified wheelset model is described. A local bifurcation analysis is performed on a non-resonant Hopf–Hopf bifurcation in Sect. 3. In Sect. 4, five near-resonant Hopf–Hopf bifurcations and the corresponding cyclic bifurcation structures are presented. Finally, Sect. 5 summarizes some conclusions.

2 The simplified railway wheelset model

In our study of Hopf–Hopf bifurcation, we shall review a two-dimensional system of the simplified railway wheelset model discussed by Yabuno et al. [9], as follows:

$$\begin{cases} \frac{d^2y}{dt^2} = -\frac{2\kappa_y}{mv}\frac{dy}{dt} - \frac{k_x}{m}\left(1-\frac{l_0}{l}\right)y + \frac{2\kappa_y}{m}\psi, \\ \frac{d^2\psi}{dt^2} = -\frac{2d_0^2\kappa_x}{Iv}\frac{d\psi}{dt} - \frac{2d_0\kappa_x\gamma_e}{Ir_0}y - \frac{k_x d_1^2}{I}\psi. \end{cases} \tag{1}$$

The lateral displacement and yaw motion variable are presented by y and ψ, respectively. The mechanical model as well as symbols of the wheelset and track are shown in Fig. 1. An illustration is supplied and

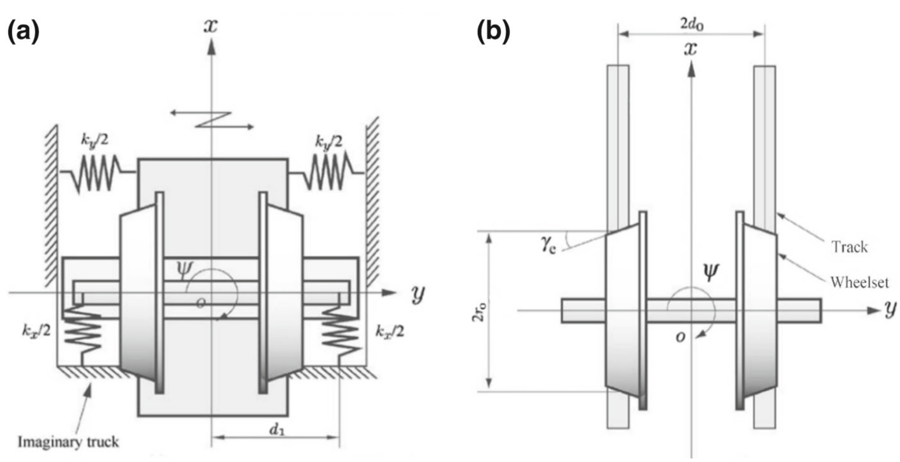

Fig. 1 **a** The schematic of wheelset with elastic joints. **b** Configuration of the wheelset and rails. The description and values of the symbols are listed in Table 1. These graphics are from [10]

Table 1 Values of the parameters in Eq. (1)

Notations	Description	Value
m	Mass of the wheelset	2.13 kg
I	Moment of inertia	0.00347 kg·m^2
υ	Train speed	−m/s(km/h)
l	Length of the spring in the equilibrium state	0.056 m
l_0	Natural length of the spring	0.035 m
$k_x(k_y)$	Longitudinal (lateral) suspension stiffness	180 N/m (variable)
d_0	Half of track gauge	0.049 m
r_0	Centered wheel rolling radius	0.036 m
γ_e	Wheel tread angle (slope of conical wheel)	0.025
$\omega_y(\omega_\psi)$	Natural frequency in lateral (yawing) direction	19.0 rad/s (35.0 rad/s)
$\kappa_x(\kappa_y)$	Longitudinal (lateral) creep coefficient	180 N (144 N)
d_1	Half of spring spacing (lateral)	0.075 m

several physical notations as well as the corresponding parameter values are labeled in Table 1.

According to the center manifold theory and bifurcation theory of limit cycles [1,2], the cubic and odd nonlinear terms decide the occurrence of hunting motion induced by Hopf bifurcation. In order to analyze the Hopf bifurcation type and bifurcation structure of cycles, the third-order terms in the wheelset model must be considered. The dimensionless transformations $y = d_0 y^*$, $t = t^*/\omega_\psi$ and $\upsilon = d_0\omega_\psi \upsilon^*$ are used to derive a nonlinear wheelset motion model described in [9]

$$\begin{cases} \ddot{y}^* + \frac{d_{11}}{\upsilon^*}\dot{y}^* + (k_{11} + k_{a11})y^* + k_{12}\psi + \alpha_{yyy}y^{*3} \\ \quad +\alpha_{yy\psi}y^{*2}\psi + \alpha_{y\psi\psi}y^*\psi^2 + \alpha_{\psi\psi\psi}\psi^3 = 0, \\ \ddot{\psi} + \frac{d_{22}}{\upsilon^*}\dot{\psi} + k_{21}y^* + k_{22}\psi + \beta_{yyy}y^{*3} \\ \quad +\beta_{yy\psi}y^{*2}\psi + \beta_{y\psi\psi}y^*\psi^2 + \beta_{\psi\psi\psi}\psi^3 = 0. \end{cases} \tag{2}$$

These eight nonlinear coefficients, $\alpha_{yyy}, \ldots, \alpha_{\psi\psi\psi}$, are given in some References [9,10,13–15]. These cubic nonlinear terms include factors such as the nonlinear effects owing to kinematics of the contact points, mechanical suspension, and creepage-creep forces determined by Kalker's theory. In addition, the elements of Eq. (2) are represented as follows:

$$d_{11} = \frac{2\kappa_y}{md_0\omega_\psi^2}, \quad d_{22} = \frac{2\kappa_x d_0}{I\omega_\psi^2}, \quad k_{21} = \frac{2d_0^2\kappa_x\gamma_e}{Ir_0\omega_\psi^2},$$
$$\upsilon^* = \frac{\upsilon}{d_0\omega_\psi},$$
$$k_{12} = \frac{-2\kappa_y}{md_0\omega_\psi^2}, \quad k_{22} = \frac{k_x d_1^2}{I\omega_\psi^2}, \quad k_{a11} = \frac{k_y}{m\omega_\psi^2},$$
$$k_{11} = \frac{k_x(1 - l_0/l)}{m\omega_\psi^2}.$$

where υ^* is the dimensionless running speed of vehicle, d_{11} is the ratio of the creep coefficient in lateral and the primary spring stiffness of longitudinal, k_{11} is the ratio of the primary spring stiffness of lateral and the primary spring stiffness of longitudinal, and k_{22} is the ratio of the longitudinal suspension stiffness and the square of natural frequency in yawing direction. These dimensionless coefficients are shown in Table 2.

With the change of variables $(y_1, y_2, y_3, y_4)^T = (y^*, \dot{y}^*, \psi, \dot{\psi})^T$, then (2) turns into

$$\dot{y_1} = y_2,$$

Table 2 Values of the parameters in Eq. (2)

k_{12}	k_{21}	k_{a11}	d_{22}	υ^*	α_{yyy}	$\alpha_{yy\psi}$	$\alpha_{y\psi\psi}$	$\alpha_{\psi\psi\psi}$	β_{yyy}	$\beta_{yy\psi}$	$\beta_{y\psi\psi}$	$\beta_{\psi\psi\psi}$
−2.26	−0.375	0.7	−2.26	4.4328	0.4	0.4	0.5	0.7	0.6	0.4	0.9	0.6

$$\dot{y_2} = -\frac{d_{11}}{\upsilon^*} y_2 - (k_{11} + k_{a11}) y_1 - k_{12} y_3 - \alpha_{yyy} y_1^3 - \alpha_{yy\psi} y_1^2 y_3 - \alpha_{y\psi\psi} y_1 y_3^2 - \alpha_{\psi\psi\psi} y_3^3,$$
$$\dot{y_3} = y_4,$$
$$\dot{y_4} = -\frac{d_{22}}{\upsilon^*} y_4 - k_{21} y_1 - k_{22} y_3 - \beta_{yyy} y_1^3 - \beta_{yy\psi} y_1^2 y_3 - \beta_{y\psi\psi} y_1 y_3^2 - \beta_{\psi\psi\psi} y_3^3. \quad (3)$$

The Jacobian matrix of (3) evaluated at the equilibrium $(y_1^*, y_2^*, y_3^*, y_4^*)^T = (0, 0, 0, 0)^T$ is given by

$$R = \begin{pmatrix} 0 & 1 & 0 & 0 \\ -k_{11} - k_{a11} & -\frac{d_{11}}{\upsilon^*} & -k_{12} & 0 \\ 0 & 0 & 0 & 1 \\ -k_{21} & 0 & -k_{22} & -\frac{d_{22}}{\upsilon^*} \end{pmatrix}$$

and the characteristic polynomial $P(\lambda)$ is

$$P(\lambda) = q_0\lambda^4 + q_1\lambda^3 + q_2\lambda^2 + q_3\lambda + q_4.$$

where

$$\begin{aligned} q_0 &= 1 \\ q_1 &= \tfrac{1}{\upsilon^*}(d_{11} + d_{22}) \\ q_2 &= \tfrac{1}{\upsilon^{*2}} d_{11} d_{22} + k_{11} + k_{22} + k_{a11} \\ q_3 &= \tfrac{1}{\upsilon^*}(d_{11} k_{22} + d_{22}(k_{11} + k_{a11})) \\ q_4 &= k_{22}(k_{11} + k_{a11}) - k_{12} k_{21} \end{aligned} \quad (4)$$

A novel Hopf–Hopf bifurcation criterion was proposed in [16]. According to the generalization of Orlando's formula [17]

$$\Delta_{n-1} = (-1)^{n(n-1)/2} q_0^{n-1} \prod_{1 \le i < j \le n}^{1,\ldots,n} (\lambda_i + \lambda_j)$$

where

$$\Delta_{n-1} = \begin{vmatrix} q_1 & 1 & 0 \\ q_3 & q_2 & q_1 \\ 0 & q_4 & q_3 \end{vmatrix} = q_1 q_2 q_3 - q_1^2 q_4 - q_3^2, \quad \text{for} \quad n = 4.$$

the λ_i and λ_j are the roots of the polynomial $P(\lambda)$.

The non-resonant Hopf–Hopf bifurcation or resonant Hopf–Hopf bifurcation of system (2) occurs at (d_{11}^*, k_{11}^*) if and only if the following conditions (H1), (H2) and (H3) or (H1), (H2) and (H4) hold, respectively:

(H1) Eigenvalue assignment: $q_1 = 0$, $q_3 = 0$, $q_2 > 0$, $q_4 > 0$, $q_2^2 - 4q_4 > 0$.

(H2) Transversality condition:

$$\left.\frac{\partial^2(q_1 q_2 q_3 - q_1^2 q_4 - q_3^2)}{\partial d_{11}^2}\right|_{(d_{11},k_{11})=(d_{11}^*,k_{11}^*)} \neq 0,$$

$$\left.\frac{\partial^2(q_1 q_2 q_3 - q_1^2 q_4 - q_3^2)}{\partial k_{11}^2}\right|_{(d_{11},k_{11})=(d_{11}^*,k_{11}^*)} \neq 0.$$

(H3) Non-resonance condition:

$$\sqrt{\frac{q_2 - \sqrt{q_2^2 - 4q_4}}{2}} \Bigg/ \sqrt{\frac{q_2 + \sqrt{q_2^2 - 4q_4}}{2}} \neq \frac{m}{n},$$

where m and n are relatively prime, such that $m + n \le 5$.

(H4) Resonance condition:

$$\sqrt{\frac{q_2 - \sqrt{q_2^2 - 4q_4}}{2}} \Bigg/ \sqrt{\frac{q_2 + \sqrt{q_2^2 - 4q_4}}{2}} = \frac{m}{n},$$

where m and n are relatively prime, such that $m + n \le 5$.

3 Local dynamical analysis

In the principal bifurcation parameter space (d_{11}, k_{11}, k_{22}), the mathematical model related to the simplified railway wheelset model (3) undergoes a Hopf–Hopf bifurcation along the curve defined by

$$HH = \left\{ (d_{11}, k_{11}, k_{22}) : d_{11} = -d_{22}, k_{11} = k_{22} - k_{a11}, k_{22} \le \frac{k_{12} k_{21} \upsilon^{*2}}{d_{22}^2} + \frac{d_{22}^2}{4\upsilon^{*2}} \right\}. \quad (5)$$

The ratio of two frequencies ω_1 and ω_2 at the Hopf–Hopf singularity points is revealed in Fig. 2a, and the Hopf–Hopf singularity points regarding six distinct k_{22} are shown in Fig. 2b. For simplicity, these singularity points are denoted from top to bottom as $HH_{1:1}$, $HH_{2:3}$, $HH_{1:2}$, HH_{non}, $HH_{1:3}$, $HH_{1:4}$ throughout the paper. Two "independent" Hopf bifurcation curves H_1 and H_2 exist on every curve in Fig. 2b caused by two distinct pairs of conjugated purely imaginary eigenvalues pass transversally through the imaginary axis, the corresponding frequencies are ω_1 and ω_2, respectively.

The four-dimensional normal form of the wheelset model can be reduced to a two-dimensional amplitude system given by [1,18]

$$\begin{cases} \dot{\xi_1} = \xi_1(\mu_1 + \xi_1 - \theta\xi_2 + \Theta\xi_2^2) \\ \dot{\xi_2} = \xi_2(\mu_2 + \delta\xi_1 - \xi_2 + \Delta\xi_1^2) \end{cases} \quad (6)$$

where the state variables $\xi_{1,2}$ represent the amplitude of the emerging limit cycles, $\xi_1 = p_{11}\rho_1$, $\xi_2 = p_{22}\rho_2$,

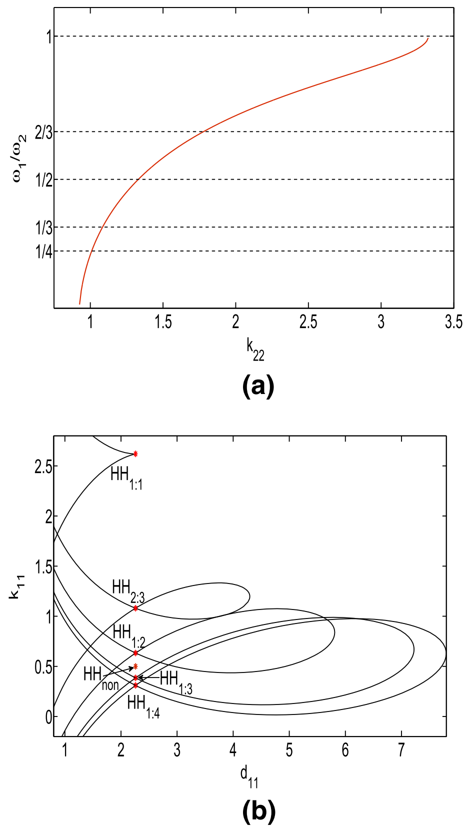

Fig. 2 **a** The ratio of frequencies ω_1 and ω_2 on the Hopf–Hopf curve as a function of k_{22}. **b** Hopf curves with five distinctive values of k_{22} ($k_{22} = 3.322$, 1.78, 1.332, 1.084 and 1.01) in the parameter plane (d_{11}, k_{11})

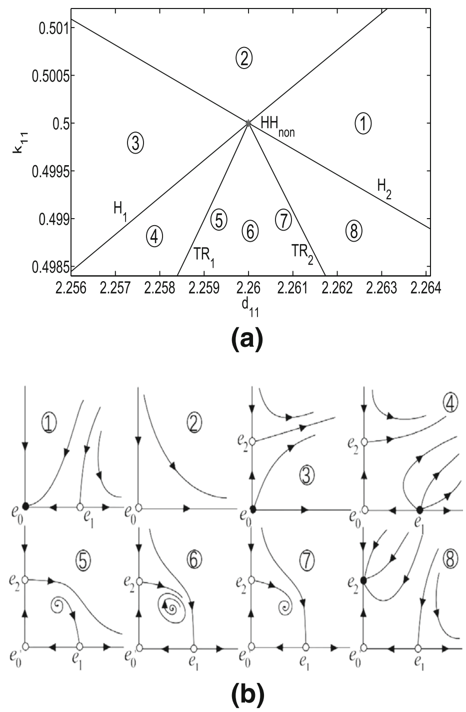

Fig. 3 **a** Parametric portraits associated with the truncated normal form of the Hopf–Hopf bifurcation for $p_{11} \cdot p_{22} < 0$ ($k_{22} = 1.2$). **b** Phase diagram of region ①–⑧ in **a**

p_{11} and p_{22} are real coefficients, $\mu_{1,2}$ are the bifurcation parameters.

All the continuations were implemented with MATCONT [19]. Computing the coefficients of the truncated normal form of the Hopf–Hopf bifurcation with MATCONT results in $p_{11} \cdot p_{22} = -1, \theta = -2, \delta = -2, \Theta = 603.568, \Delta = -406.0986$. Note that the truncated normal form excludes resonance conditions of m/n. The parametric portrait belongs to the "difficult" case VI and the dynamics presented by the phase portraits can be translated to the wheelset model, as depicted in Fig. 3.

The point e_0 of the amplitude system Eq.(6) is the equilibrium point at the origin of system Eq.(3), the equilibria e_1 and e_2 are the limit cycles born at the Hopf curves H_1 and H_2 in Fig. 3a, respectively, which are formally the same as in the "simple" case and coincide with the coordinate axes. The nontrivial equilibrium e_3 collides with e_1 and e_2 at the Neimark–Sacker curves TR_1 and TR_2, respectively, but e_3 undergoes a Hopf bifurcation, the emerging limit cycle vanishes at a heteroclinic bifurcation, which are not shown in Fig. 3a since the implemented algorithms on the numerical continuation package do not calculate bifurcation of torus [20].

The associated phase diagrams [1] near the non-resonant Hopf–Hopf singularity point HH_{non} at $d_{11}^* = 2.26$ and $k_{11}^* = 0.50$ (detected at $k_{22} = 1.2$) are presented in Fig. 3b. In region ②, the equilibrium e_0 is unstable and it is the only local limit set. In region ③, the unstable limit cycle produced by the Hopf bifurcation H_2 coexists with equilibrium e_0. Within region ④, another unstable limit cycle is created by means of H_1. An unstable 2D torus is created by the Neimark–Sacker bifurcation TR_1 in region ⑤. In region ⑥, the unstable 2D torus of region ⑤ undergoes a heteroclinic bifurcation, resulting in a stable 3D torus. Increasing the value of d_{11} will make the 3D torus collapse and the 2D torus stabilize in region ⑦. Subsequently, the stable 2D torus collapses on the Neimark–Sacker bifurcation TR_2 and two stable limit cycles coexist (region ⑧).

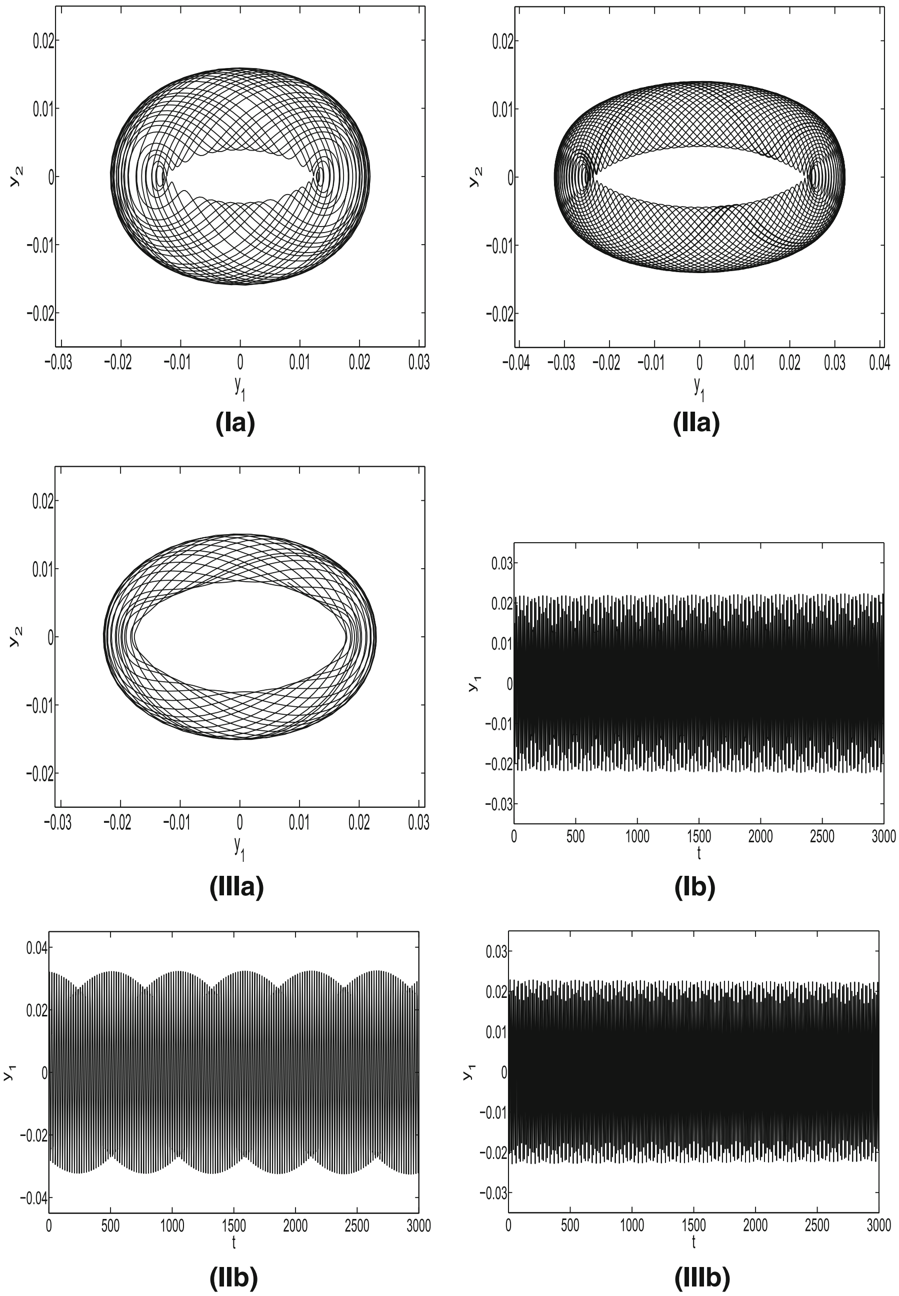

Fig. 4 (I) Unstable 2D torus present in region ⑤. (II) Stable 3D torus located in region ⑥. (III) Stable 2D torus related to regions ⑦

Within region ①, one of the stable limit cycles vanishes at the Hopf curve H_2 and the equilibrium e_0 at the origin turns stable. Crossing the Hopf curve H_1, the scheme returns to the initial place in the region ②.

The phase diagrams corresponding to the three situations of region ⑤–⑦ are presented in Fig. 4(Ia)–(IIIa), (Ib)–(IIIb) show the waveform diagrams of the three distinct torus corresponding to Fig. 4(Ia)–(IIIa), respectively. The location of the projection of the unstable 2D torus on the plane y_1–y_2 is $(d_{11}, k_{11}) = (2.25970, 0.49995)$, the position of the stable 3D torus is $(d_{11}, k_{11}) = (2.25990, 0.49995)$ and the site of stable 2D torus is $(d_{11}, k_{11}) = (2.26010, 0.49995)$.

Table 3 Labels and colors of bifurcation curves used in the figures

Bifurcation curve	Hopf	Cyclic fold	Neutral Saddle	Neimark–Sacker
Label	H	LPC	NS	TR
Color	Black	Red	Yellow	Blue

4 "Nonlocal" dynamical analysis near the resonant Hopf–Hopf bifurcation

In this section, several near-resonant Hopf–Hopf bifurcations are performed by means of numerical continuation methods. Bifurcation diagrams in the parameter plane (d_{11}, k_{11}) are shown for five distinct values of k_{22}, namely $k_{22} = 3.322$, 1.78, 1.332, 1.084 and 1.01, corresponding to the Hopf–Hopf bifurcation near 1:1, 2:3, 1:2, 1:3 and 1:4 resonance, respectively. The labels and colors of several bifurcation curves used in the figures are presented in Table 3.

The first Lyapunov coefficient (*FLC*) and the second Lyapunov coefficient (*SLC*) are applied to judge the type of Hopf bifurcation. The index $c(0)$ denotes normal form coefficients of cyclic fold bifurcation, cyclic cusp bifurcation and cyclic Neimark–Sacker bifurcation. Furthermore, when Chenciner bifurcation is nondegenerate [1], the coefficient of the resonant cubic term $Re(e)$ is nonzero, two positive fixed points with opposite stability exist in the vicinity of the origin. If $Re(e) < 0$, the outer one of the two fixed points is stable. If $Re(e) > 0$, the inner one is stable.

4.1 Parameter values close to the 1:1 resonant Hopf–Hopf bifurcation condition

The focus in this section is to explore the dynamics near the 1:1 resonant Hopf–Hopf bifurcation when $k_{22} = 3.322$. The Hopf–Hopf singularity point $HH_{1:1}$ is located at $d_{11}^* = 2.260007$ and $k_{11}^* = 2.622000$. The frequencies of the Hopf bifurcation curves $H_{1,2}$ can be detected in Matcont, where $\omega_1 = 1.77824$, $\omega_2 = 1.79497$ and thus the frequency ratio $\omega_1 : \omega_2 \approx 0.9907$, which is quite close to 1:1 resonant condition. Two generalized Hopf bifurcation points $GH_{1,2}$ (see Fig. 5a) such that the index *FLC* vanishes emerge on the Hopf curves $H_{1,2}$, respectively, as shown below:

$$GH_1,\ d_{11} = 2.197291,\ k_{11} = 2.613999,$$
$$\text{Period}_1 = 3.033659,\ \text{SLC} = -0.5111842,$$

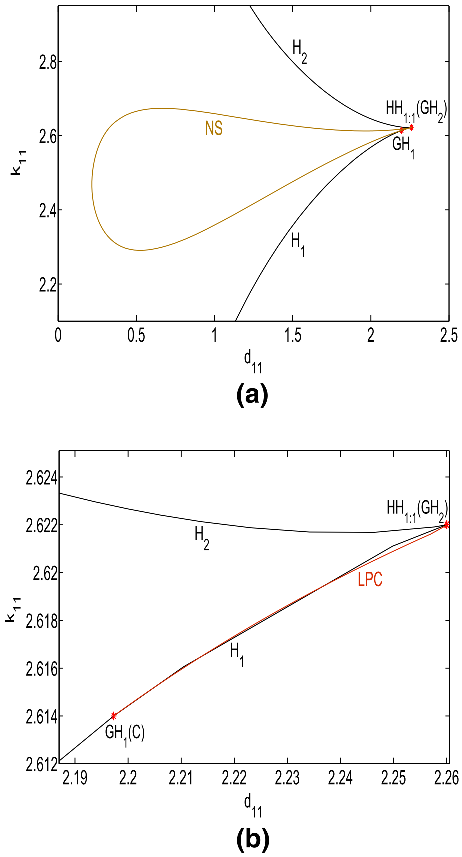

Fig. 5 **a** Bifurcation diagram for $k_{22} = 3.322$ near the 1:1 resonant Hopf–Hopf bifurcation. **b** Expanded view close to the singularity point $HH_{1:1}$ for $(d_{11}^*, k_{11}^*) = (2.260007, 2.622000)$

$$GH_2,\ d_{11} = 2.262327,\ k_{11} = 2.622129,$$
$$\text{Period}_2 = 3.196912,\ \text{SLC} = 29575.65.$$

As presented in Fig. 5b, the point GH_1 where the cyclic fold curve LPC appears is a generalized Hopf bifurcation point such that the index *FLC* is zero, the curve LPC runs very close to the Hopf curve H_1 and is connected to GH_2, in particular, GH_2 can be detected in the vicinity of $HH_{1:1}$. The cyclic cusp point C emerging on LPC is near to GH_1, which is located at $d_{11} = 2.197297$ and $k_{11} = 2.614000$.

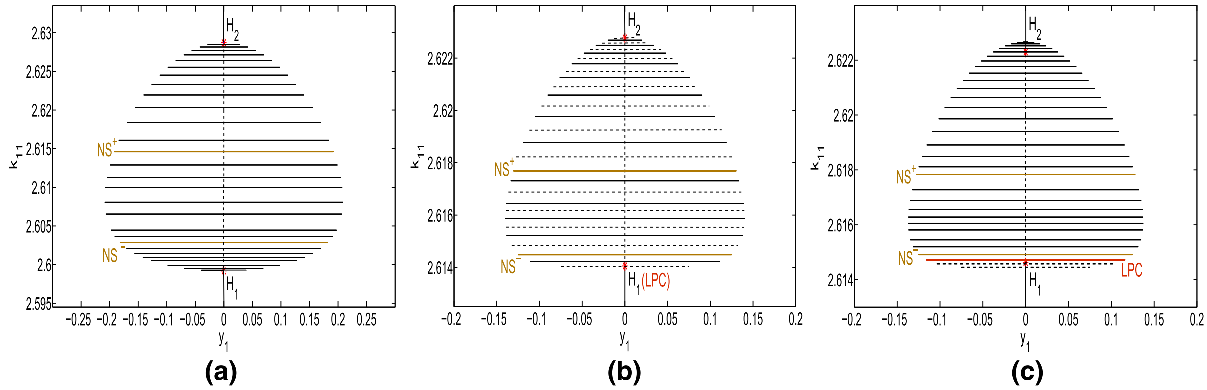

Fig. 6 **a–c** Bifurcation structures for $d_{11} = 2.12, 2.197291$ (GH_1), 2.20, respectively. The black solid curves denote stable equilibria and stable limit cycles, the black dotted curves indicate unstable equilibria and unstable limit cycles, the yellow and red curves signify cyclic neutral saddles and cyclic limit points, respectively. (Color figure online)

In this case, both the Hopf curves $H_{1,2}$ intersect at $HH_{1:1}$ and do not form a closed loop. In addition, a neutral saddle curve NS born at $HH_{1:1}$ forms a closed curve and returns to the initial place. In addition, the global bifurcation scenario near the 1:1 resonant Hopf–Hopf bifurcation is not involved in cyclic Neimark–Sacker bifurcation.

In Fig. 5b, taking GH_1 as a dividing point, the supercritical Hopf bifurcation happens on the left of GH_1 and the subcritical Hopf bifurcation happens on the right side. Corresponding to distinct d_{11}, the coexistence of equilibria and limit cycles detected between two Hopf bifurcation points $H_{1,2}$ is shown in Fig. 6a–c, and their bifurcation values are listed in Table 4. The limit cycles born at the supercritical Hopf bifurcation point ($FLC < 0$) are stable. The limit cycles born at the subcritical Hopf bifurcation point ($FLC > 0$) are unstable. The negative normal form coefficient $c(0)$ indicates that the limit cycles born at the cyclic limit point are stable. The positive index $c(0)$ indicates that the limit cycles born at the cyclic limit point are unstable. In particular, if the cyclic limit point LPC coincides with GH_1, the index $c(0)$ is equal to 0.

In Fig. 7, the cyclic bifurcation behaviors undergo a cyclical process, which is portrayed between two Hopf bifurcation points $H_{1,2}$. When $d_{11} = 2.1$, the cyclic bifurcation structure in 2D plane is displayed in Fig. 7a, and a stereoscopic bifurcation structure in 3D space is exhibited in Fig. 7b. Due to the index $FLC = -0.03513515$, a family of stable limit cycles are arisen from H_1 at $k_{11} = 2.594947$. As k_{11} increases, the limit cycles finally reach H_2 after undergoing two cyclic neutral saddles $NS^{\pm}$. The negative index $FLC = -0.1331188$ indicates the stability of the limit cycles born at H_2 remains unchanged.

In addition, the cyclical process between two Hopf bifurcation points $H_{1,2}$ is shown as: $H_1 \xrightarrow{SC} NS^- \xrightarrow{SC} NS^+ \xrightarrow{SC} H_2 \xrightarrow{SC} NS^+ \xrightarrow{SC} NS^- \xrightarrow{SC} H_1$. (Here, SC denotes stable limit cycles portrayed by black solid curves). The loop indicates that the stable limit cycles generated by the wheelset coexist within the region of H_1 and H_2.

Table 4 Labels and colors of bifurcation curves used in the figures

Figure	$d_{11}(H_1/H_2)$	$FLC(H_1)$	$FLC(H_2)$	$k_{11}(LPC)$	$c(0)$
Figure 6a	2.12	−0.03104245	−0.1375144	–	–
Figure 6b	2.197291	0.000027251	−0.1677935	2.613999	0.000011564
Figure 6c	2.20	0.002115517	−0.1696833	2.614436	−0.0048517

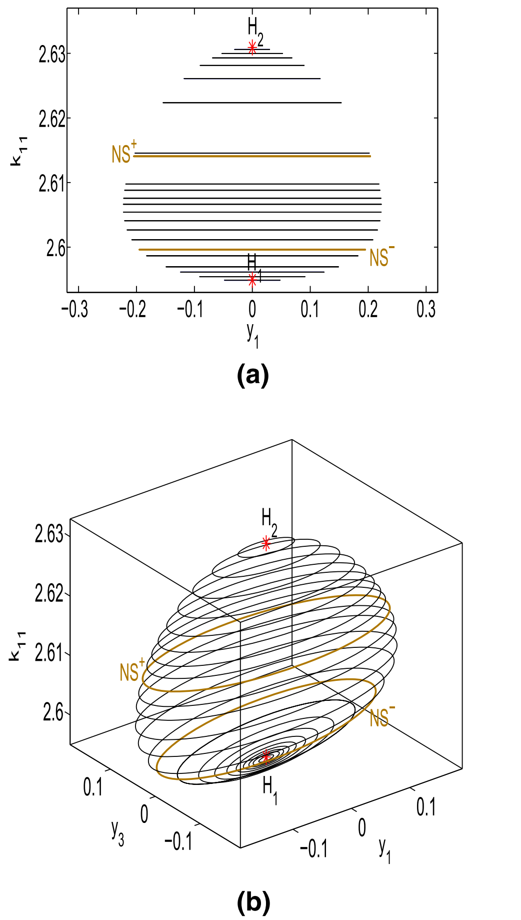

Fig. 7 **a** Cyclic bifurcation structure for $d_{11} = 2.1$ and $k_{22} = 3.322$ on 2D plane. The black solid curves indicate stable limit cycles, the yellow curves signify cyclic neutral saddles. **b** Cyclic bifurcation structure in 3D space corresponds to the labels in **a**. (Color figure online)

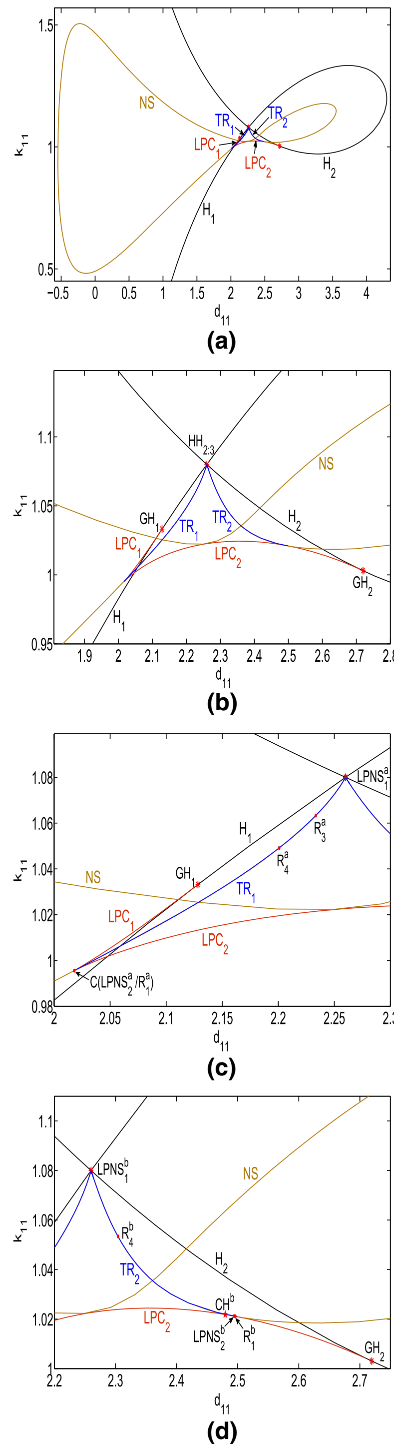

Fig. 8 **a** Bifurcation diagram for $k_{22} = 1.78$ near the 2:3 resonant Hopf–Hopf bifurcation. **b** Magnified view close to the singularity point $\text{HH}_{2:3}$ for $(d_{11}^*, k_{11}^*) = (2.259995, 1.079998)$. **c** Bifurcation diagram associated with the Neimark–Sacker bifurcation curve TR_1. **d** Bifurcation diagram related to the Neimark–Sacker bifurcation curve TR_2

4.2 Parameter values close to the 2:3 resonant Hopf–Hopf bifurcation condition

In order to analyze the Hopf–Hopf bifurcation close to 2:3 resonance, as presented in Fig. 8a, k_{22} is fixed at 1.78. The singularity point $\text{HH}_{2:3}$ is located at $d_{11}^* = 2.259995$ and $k_{11}^* = 1.079998$. In the present case, the frequencies $\omega_1 = 1.0080, \omega_2 = 1.5112$, i.e., $\omega_1 : \omega_2 \approx 0.6670$ is relatively close to the 2:3 resonant condition.

The dynamic scene near the 2:3 resonant Hopf–Hopf singularity point can qualitatively describe the complexity of this case. The detection of two Neimark–Sacker branches $\text{TR}_{1,2}$ and two cyclic fold curves $\text{LPC}_{1,2}$ are shown in the magnified view of Fig. 8b. Two distinct Neimark–Sacker bifurcation structures $\text{TR}_{1,2}$

associated with the Hopf curves $H_{1,2}$ can be clearly determined. One of the outstanding features is that the branches $TR_{1,2}$ are connected by a neutral saddle curve NS to form a closed curve starting and ending at $HH_{2:3}$.

The two points where the curves $LPC_{1,2}$ emerge are generalized Hopf bifurcation points $GH_{1,2}$ such that the index FLC vanishes, which are involved in the connection of the cyclic fold curves. Specifically, the coordinates and properties of the points $GH_{1,2}$ (see Fig. 8b) are as follows:

$$\begin{aligned} &GH_1,\ d_{11} = 2.128304,\ k_{11} = 1.033156, \\ &\quad Period_1 = 0.976125,\ SLC = 0.09138855, \\ &GH_2,\ d_{11} = 2.719480,\ k_{11} = 1.003051, \\ &\quad Period_2 = 2.158481,\ SLC = 0.05694257. \end{aligned}$$

In addition, both the curves $LPC_{1,2}$ encounter each other where a cyclic cusp point C: $(d_{11}, k_{11}) = (2.017879, 0.9955397)$ with $c(0) = 11762.70$ appears, as indicated in Fig. 8c. Moreover, a 1:1 resonance point R_1^a near to C is detected on the curve LPC_1, this cycle has a double Floquet multipliers with $\mu_{1,2} = 1$ at this singularity point.

The bifurcation diagram related to the branch TR_1 is presented in Fig. 8c, a couple of Fold-Neimark–Sacker points, denoted as $LPNS^a_{1,2}$, located near the ends of TR_1. Moreover, there is a 1:3 resonance point (two Floquet multipliers at $e^{\pm i(2\pi/3)}$) and a 1:4 resonance point (two Floquet multipliers at $e^{\pm i(\pi/2)}$) on the branch TR_1, denoted as R_3^a and R_4^a, respectively. Finally, the branch TR_1 ends at R_1^a and connects the curve NS. As mentioned for R_1^a, which is on both the curves TR_1 and LPC_1, and divides this curve into TR_1 and NS.

In Fig. 8d, a Fold-Neimark–Sacker point $LPNS_1^b$ is detected in the vicinity of $HH_{2:3}$, which is similar to $LPNS_1^a$ on the branch TR_1. A Chenciner bifurcation point CH^b: $(d_{11}, k_{11}) = (2.480187, 1.021899)$ with $Re(e) = -86.50386$ is situated on TR_2 related to the limit cycle emanated from the Hopf curve H_2, thus the outer fixed point is stable and the inner one is unstable. Moreover, a 1:4 resonance point R_4^b is observed here. Ultimately, the branch TR_2 ends at a 1:1 resonance point R_1^b near to another point $LPNS_2^b$.

In general, the Neimark–Sacker branch TR_1 born at the singularity point $HH_{2:3}$ connects the neutral saddle curve NS after reaching the 1:1 resonance point R_1^a. Then NS arrives at R_1^b after two turns, which is connected to the Neimark–Sacker branch TR_2, and finally forms a closed curve.

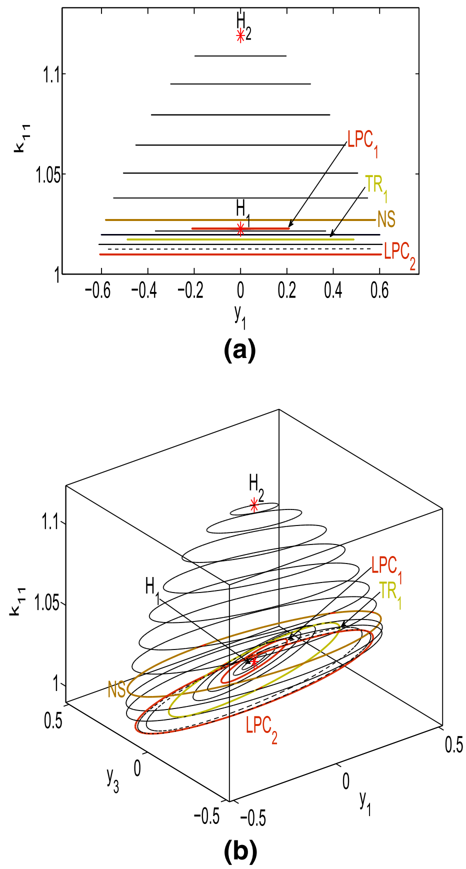

Fig. 9 **a** Cyclic bifurcation structure for $d_{11} = 2.1$ and $k_{22} = 1.78$ on 2D plane. The black solid curves stand for stable limit cycles and the black dashed curves stand for unstable ones. The red, yellow and green curves stand for cyclic limit points, cyclic neutral saddles and cyclic Neimark–Sacker bifurcation points, respectively. The labels and types corresponding to the following situations have the same implications. **b** Cyclic bifurcation structure in 3D space with respect to the labels in **a**. (Color figure online)

In Fig. 9, the same parameter d_{11} is fixed at 2.1 to continue k_{11} and to observe the cyclic bifurcation behaviors. Due to the negative index $FLC = -0.004220202$, thus the limit cycles born at H_1 are stable. As k_{11} increases, the stability of limit cycles remains unchanged when undergoing a cyclic limit point LPC_1 with normal form coefficient $c(0) = -0.003745364$. Subsequently, due to the positive index $c(0) = 0.0001374898$, a series of limit cycles become unstable when a double complex Floquet multipliers are outside the unit circle, which indicates that an unstable torus is created via a cyclic Neimark–Sacker bifurcation point TR_1. The limit cycles restore stability until the point LPC_2 with $c(0) = -0.1138517$ emerges and then a cyclic neutral saddle NS is detected. Ultimately, the limit cycles return to the point H_2 with $FLC = -0.05211610$ and start a recurrence.

Between two Hopf bifurcation points $H_{1,2}$, the loop in the process of numerical simulation can be shown as: $H_1 \xrightarrow{SC} LPC_1 \xrightarrow{SC} TR_1 \xrightarrow{UC} LPC_2 \xrightarrow{SC} NS \xrightarrow{SC} H_2 \xrightarrow{SC} NS \xrightarrow{SC} LPC_2 \xrightarrow{UC} TR_1 \xrightarrow{SC} LPC_1 \xrightarrow{SC} H_1$. (Here, SC denotes stable limit cycles portrayed by black solid curves, and UC denotes unstable limit cycles portrayed by black dotted curves). Within the region of LPC_1 and TR_1, the stable limit cycles arisen from the wheelset coexist. Within the region of TR_1 and LPC_2, the stable limit cycles arisen at LPC_2 coexist with unstable limit cycles born at TR_1, which indicates the presence of an unstable torus.

4.3 Parameter values close to the 1:2 resonant Hopf–Hopf bifurcation condition

A global unfolding of the Hopf–Hopf bifurcation near 1:2 resonance is depicted in Fig. 10a, the singularity point $HH_{1:2}$ at $d_{11}^* = 2.260000$ and $k_{11}^* = 0.632000$ appears when $k_{22} = 1.332$. The ratio of both frequencies $\omega_1 = 0.694406$ and $\omega_2 = 1.38631$ is approximately 0.5009, which satisfies the resonant condition close to 1:2. This kind of connection of a neutral saddle curve NS and two Neimark–Sacker branches $TR_{1,2}$ is similar to the case near 2:3 resonance. Two generalized Hopf bifurcation points $GH_{1,2}$ (see Fig. 10b) emerge on two Hopf bifurcation curves $H_{1,2}$, respectively, noted as

$$
\begin{aligned}
&GH_1,\ d_{11} = 2.133968,\ k_{11} = 0.582715,\\
&\quad \text{Period}_1 = 0.448234,\ SLC = 0.1660530,\\
&GH_2,\ d_{11} = 2.857789,\ k_{11} = 0.511944,\\
&\quad \text{Period}_2 = 1.785885,\ SLC = 0.04155471.
\end{aligned}
$$

A similar scenario observed is that the curves $LPC_{1,2}$ born at $GH_{1,2}$ intersect at a cusp point, this point is detected at C: $(d_{11}, k_{11}) = (1.970543, 0.5222585)$ with $c(0) = 11888.44$. For the 1:1 resonance point R_1^a near to C, as depicted in Fig. 10c, is encountered on both the curves LPC_1 and TR_1.

The bifurcation diagram of the semi-structure related to the branch TR_1 is exhibited in Fig. 10c. Compared with the Hopf–Hopf bifurcation near 2:3 resonance, more strong resonances such as two 1:3 and two 1:4

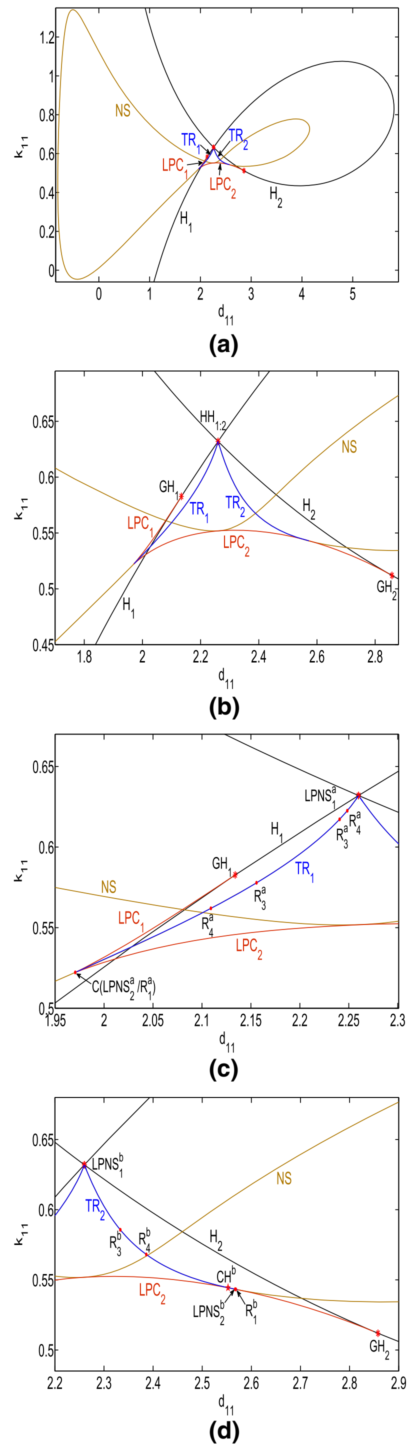

Fig. 10 **a** Bifurcation diagram for $k_{22} = 1.332$ near the 1:2 resonant Hopf–Hopf bifurcation. **b** Expanded view close to the singularity point $HH_{1:2}$ for $(d_{11}^*, k_{11}^*) = (2.260000, 0.632000)$. **c** Bifurcation diagram associated with the Neimark–Sacker bifurcation curve TR_1. **d** Bifurcation diagram related to the Neimark–Sacker bifurcation curve TR_2

resonance points are detected, denoted as R_3^a and R_4^a, respectively. In addition, the same scenario as both the branches TR_1 is the presence of the points $LPNS_{1,2}^a$, TR_1 intersects with LPC_1 at a 1:1 resonance point R_1^a and ends with this point.

The dynamics of the semi-structure associated with the branch TR_2 is illustrated in Fig. 10d . The backward numerical continuation produces one Fold-Neimark–Sacker point $LPNS_1^b$ close to $HH_{1:2}$, and the other $LPNS_2^b$ near to R_1^b is created by the forward numerical continuation. Among them, a 1:4 resonance point R_4^b is observed near the curve NS, a Chenciner bifurcation point CH^b: $(d_{11}, k_{11}) = (2.552513, 0.5444179)$ with $Re(e) = -137.8334$ emerges on the branch TR_2. Compared with the case near 2:3 resonance, the similar scenario of two Neimark–Sacker branches TR_2 are that both generate a point CH^b and a couple of points $LPNS_{1,2}^b$, and end in a 1:1 resonance point R_1^b. However, the discrepancy is the presence of a 1:3 resonance point R_3^b.

Analogously, the parameter d_{11} is fixed at 2.1 to observe the cyclic bifurcation behaviors when k_{11} changes in Fig. 11. The structure similar to the Hopf–Hopf bifurcation near 2:3 resonance occurs in the process of numerical continuation, just like the above analysis. The inner Hopf bifurcation point H_1 with $FLC = -0.005551508$ and the outer one H_2 with $FLC = -0.05254251$ indicate that the limit cycles born at $H_{1,2}$ are both stable. Two cyclic limit points are detected at LPC_1 with $c(0) = -0.001739350$ and LPC_2 with $c(0) = -0.1104969$. A series of unstable limit cycles exist till a Neimark–Sacker bifurcation point labeled by TR_1 is encountered at $k_{11} = 0.5591471$, at which a positive index $c(0)$ reveals that an unstable torus is created. The presence of a cyclic neutral saddle NS is located between H_2 and LPC_2.

An analogous loop between two Hopf bifurcation points $H_{1,2}$ can be exhibited as: $H_1 \xrightarrow{SC} LPC_1 \xrightarrow{SC} TR_1 \xrightarrow{UC} LPC_2 \xrightarrow{SC} NS \xrightarrow{SC} H_2 \xrightarrow{SC} NS \xrightarrow{SC} LPC_2 \xrightarrow{UC} TR_1 \xrightarrow{SC} LPC_1 \xrightarrow{SC} H_1$. The structure further explains that the cyclic bifurcation behaviors emanated from the wheelset are very close to the 2:3 resonant case.

4.4 Parameter values close to the 1:3 resonant Hopf–Hopf bifurcation condition

Let us investigate the unfolding of the Hopf–Hopf bifurcation near 1:3 resonance depicted in Fig. 12a, the parameter k_{22} is settled at 1.084. The singularity point $HH_{1:3}$ is situated at $d_{11}^* = 2.259999$ and $k_{11}^* = 0.384000$. The frequencies $\omega_1 = 0.436733$ and $\omega_2 = 1.31047$, i.e., $\omega_1 : \omega_2 \approx 0.3333$ is fairly close to the condition of 1:3 resonance. Two generalized Hopf bifurcation points $GH_{1,2}$ (see Fig. 12b) are shown below:

$$\begin{aligned} &GH_1,\ d_{11} = 2.138557,\ k_{11} = 0.334344,\\ &\quad \text{Period}_1 = 0.159838,\ \text{SLC} = -1.451423,\\ &GH_2,\ d_{11} = 2.941620,\ k_{11} = 0.235757,\\ &\quad \text{Period}_2 = 1.575520,\ \text{SLC} = 0.03593939. \end{aligned}$$

In this case, two cyclic fold curves arisen from $GH_{1,2}$ no longer encounter at a cusp point. The curve LPC_1^1 born at GH_1 runs very close to the Hopf bifurcation curve H_1, a 1:1 resonance point R_1^1 is observed on this curve, and a cusp point C^1: $(d_{11}, k_{11}) = (2.25999,$

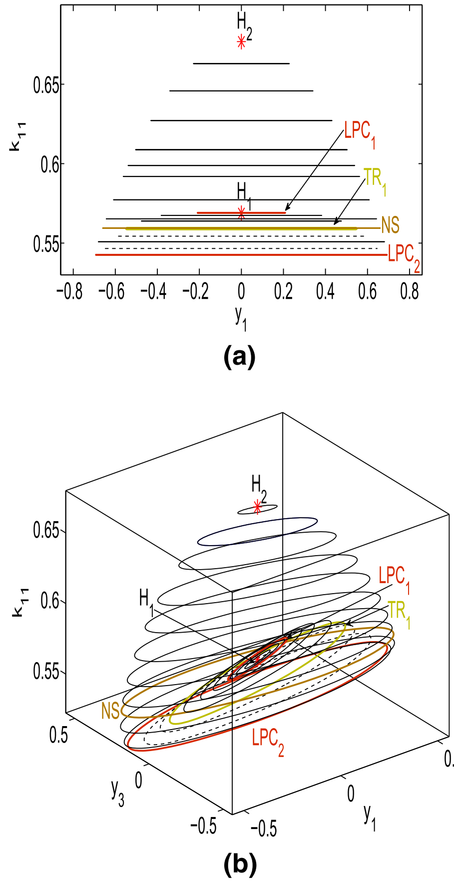

Fig. 11 **a** Cyclic bifurcation structure for $d_{11} = 2.1$ and $k_{22} = 1.332$ on 2D plane. **b** Cyclic bifurcation structure in 3D space with respect to the labels in **a**

0.383996) with $c(0) = 638.4611$ appears in the vicinity of $HH_{1:3}$, then C^1 joins the curve LPC^1_2. The curve LPC^2_1 born at GH_2 intersects the neutral saddle curve NS at a 1:1 resonance point R^a_1, then forms a cusp point C^2_1 with the curve LPC^2_2, also LPC^2_2 forms a cusp point C^2_2 with the curve LPC^2_3. Among them, these cusp points are detected at C^2_1: $(d_{11}, k_{11}) = (1.944105, 0.2595407)$ with $c(0) = 195.0080$, and C^2_2: $(d_{11}, k_{11}) = (2.007971, 0.2819056)$ with $c(0) = 0.02310147$.

The structure related to the left branch TR_1 is shown in Fig. 12c, compared with the previous two cases near 2:3 and 1:2 resonance, the discrepancy about this branch is that there is a Fold-Neimark–Sacker point $LPNS^a_1$ near to $HH_{1:3}$ and it no longer ends with a 1:1 resonance point. Furthermore, more complicated resonance phenomena consisting of more strong resonance points occur. There are a pair of 1:1, two pairs of 1:3 and two pairs of 1:4 resonance points emerging on TR_1, denoted as R^a_1, R^a_3 and R^a_4, respectively. In addition, between two resonance points R^a_1 and R^a_4, a Chenciner bifurcation point is detected at CH: $(d_{11}, k_{11}) = (2.240148, 0.3674266)$ with $Re(e) = 2.357679$, which indicates the inner fixed point is stable and the outer one is unstable.

The structure associated with the right branch TR_2 is depicted in Fig. 12d, a Chenciner bifurcation point is detected at CH: $(d_{11}, k_{11}) = (2.600987, 0.2768758)$ with $Re(e) = -207.8293$. The scenario similar to before is that a couple of Fold-Neimark–Sacker points $LPNS^b_{1,2}$ emerge and this branch ends at a 1:1 resonance point R^b_1. In particular, TR_2 produces three 1:3 resonance points R^b_3, two of which are near to $HH_{1:3}$. A 1:4 resonance point R^b_4 is observed below the curve NS and above the curve LPC^2_1.

In Fig. 13, the cyclic bifurcation behaviors are observed by keeping $d_{11} = 2.1$ unchanged and changing k_{11}. The negative index $FLC = -0.007029457$ indicates that a series of stable limit cycles are emanated from the Hopf bifurcation point H_1. When undergoing the cyclic limit point LPC^1_2, the negative index $c(0) = -3.436286$ indicates that the stable limit cycles still exist. As k_{11} decreases, the stability of limit cycles vanishes when the cyclic Neimark–Sacker point TR_1 with $c(0) = 0.0002820793$ emerges, which indicates an unstable torus is created. Then the limit cycles restore stability until LPC^2_1 with $c(0) = -0.1014374$ arises. Finally, the limit cycles return to the point H_2 after passing a cyclic neutral saddle NS.

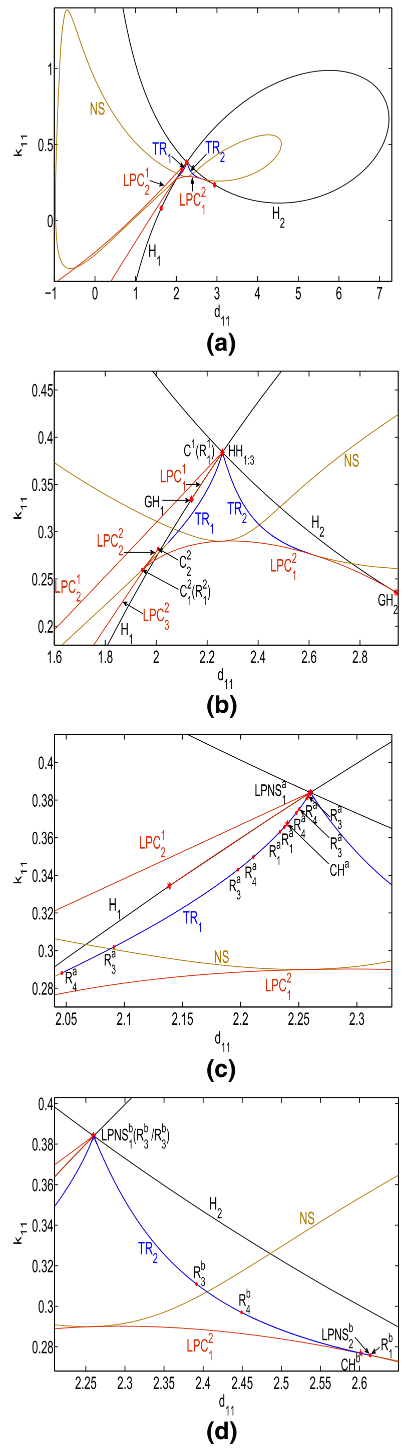

Fig. 12 **a** Bifurcation diagram for $k_{22} = 1.084$ near the 1:3 resonant Hopf–Hopf bifurcation. **b** Expanded view close to the singularity point $HH_{1:3}$ for $(d^*_{11}, k^*_{11}) = (2.259999, 0.384000)$. **c** Bifurcation diagram associated with the Neimark–Sacker bifurcation curve TR_1. **d** Bifurcation diagram related to the Neimark–Sacker bifurcation curve TR_2

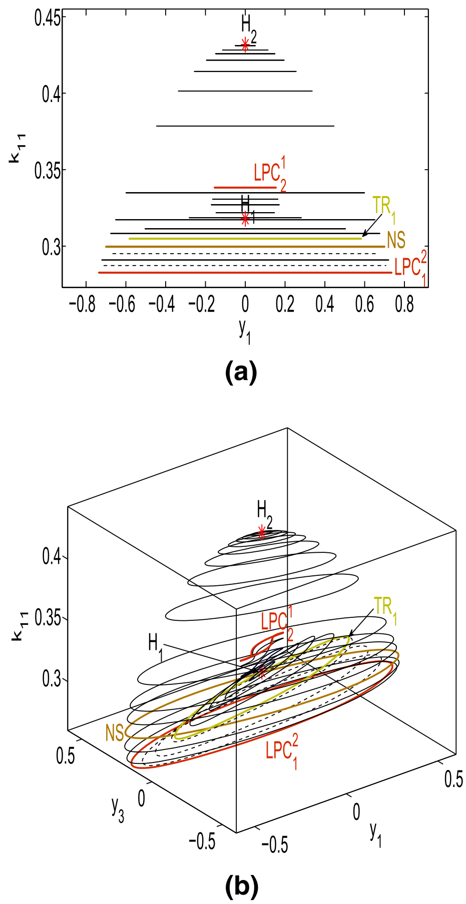

Fig. 13 **a** Cyclic bifurcation structure for $d_{11} = 2.1$ and $k_{22} = 1.084$ on 2D plane. **b** Cyclic bifurcation structure in 3D space with respect to the labels in **a**

The loop between two Hopf bifurcation points $H_{1,2}$ can be shown as: $H_1 \xrightarrow{SC} LPC_2^1 \xrightarrow{SC} TR_1 \xrightarrow{UC} LPC_1^2 \xrightarrow{SC} NS \xrightarrow{SC} H_2 \xrightarrow{SC} NS \xrightarrow{SC} LPC_1^2 \xrightarrow{UC} TR_1 \xrightarrow{SC} LPC_2^1 \xrightarrow{SC} H_1$. Within the region of LPC_2^1 and TR_1, the stable limit cycles arisen from the wheelset coexist. Within the region of TR_1 and LPC_1^2, the stable limit cycles arisen at LPC_1^2 coexist with unstable limit cycles born at TR_1, which indicates that the wheelset gives birth to an unstable torus via TR_1.

4.5 Parameter values close to the 1:4 resonant Hopf–Hopf bifurcation condition

When considering the Hopf–Hopf bifurcation near 1:4 resonance, the parameter k_{22} is set at $k_{22} = 1.01$, the singularity point $HH_{1:4}$ is located at $d_{11}^* = 2.260000$ and $k_{11}^* = 0.310000$. The frequencies $\omega_1 = 0.3228$ and $\omega_2 = 1.2868$, i.e., $\omega_1 : \omega_2 \approx 0.2508$ is quite close to the 1:4 resonant condition. Two generalized Hopf bifurcation points $GH_{1,2}$ (see Fig. 13a) are as follows:

$$GH_1,\ d_{11} = 2.140128,\ k_{11} = 0.260366,$$
$$\text{Period}_1 = 0.074224,\ \text{SLC} = -0.01398757,$$
$$GH_2,\ d_{11} = 2.967883,\ k_{11} = 0.152679,$$
$$\text{Period}_2 = 1.512267,\ \text{SLC} = 0.03449155.$$

In Fig. 14a, the condition close to the singularity point $HH_{1:4}$ leads to an extremely complicated global dynamics scenario. It is noteworthy that two neutral saddle curves $NS_{1,2}$ and three Neimark–Sacker branches $TR_{1,2,3}$ are detected, one NS_1 connects TR_1 and TR_3 and the other NS_2 connects TR_2 and TR_3, finally return to $HH_{1:4}$ after four turns. The cyclic fold curves $LPC_{1,2}^1$ and $LPC_{1,2,3}^2$ have an analogous structure in two cases compared with the Hopf–Hopf bifurcation near 1:3 resonance.

The bifurcation structure of Fig. 14c is involved in the cyclic fold curves born at GH_1. The curve LPC_1^1 forms a cusp point C_1^1 with the curve LPC_2^1, the cusp point is detected at C_1^1: (d_{11}, k_{11}) = (2.253659, 0.3048403) with $c(0) = 0.1469519$. In particular, a 1:1 resonance point R_1^a is encountered on both the curves LPC_1^1 and TR_1.

Starting from GH_2, the curve LPC_1^2 forms a cusp point C_1^2 with the second curve LPC_2^2, then LPC_2^2 ends in a cusp point C_2^2 along with the third curve LPC_3^2, which form a closed curve resembling a triangle shape, as depicted in the magnified view of Fig. 14f. These cusp points are detected at C_1^2: (d_{11}, k_{11}) = (1.934561, 0.1807090) with $c(0) = 0.09944319$, and C_2^2: (d_{11}, k_{11}) = (1.945775, 0.1843113) with $c(0) = 0.09944319$.

The substantial difference between the cases near 1:3 and 1:4 resonance lies in the cyclic fold curves $LPC_{1,2}^3$ in Fig. 14d, which contain a couple of cusp points, these cusp points are detected at C_1^3: (d_{11}, k_{11}) = (2.237032, 0.3015403) with $c(0) = -56.60203$, and C_2^3: (d_{11}, k_{11}) = (2.560117, 0.4154234) with $c(0) = 0.6525401$. Moreover, in addition to a couple of 1:1 resonance points R_1^3 on LPC_2^3, the upper part of the branch TR_3 intersects LPC_1^3 at $LPNS_1^3$, and the lower part of the branch TR_3 intersects LPC_2^3 at $LPNS_2^3$ (see Fig. 14c).

On the branch TR_1 (Fig. 14c), two 1:3 resonance points R_3^a and two 1:4 resonance points R_4^a are observed here. The Chenciner bifurcation point near LPC_1^1 is detected at CH^a: (d_{11}, k_{11}) = (2.248896, 0.3035769) with $Re(e) = 131.4880$. A couple of Fold-Neimark–

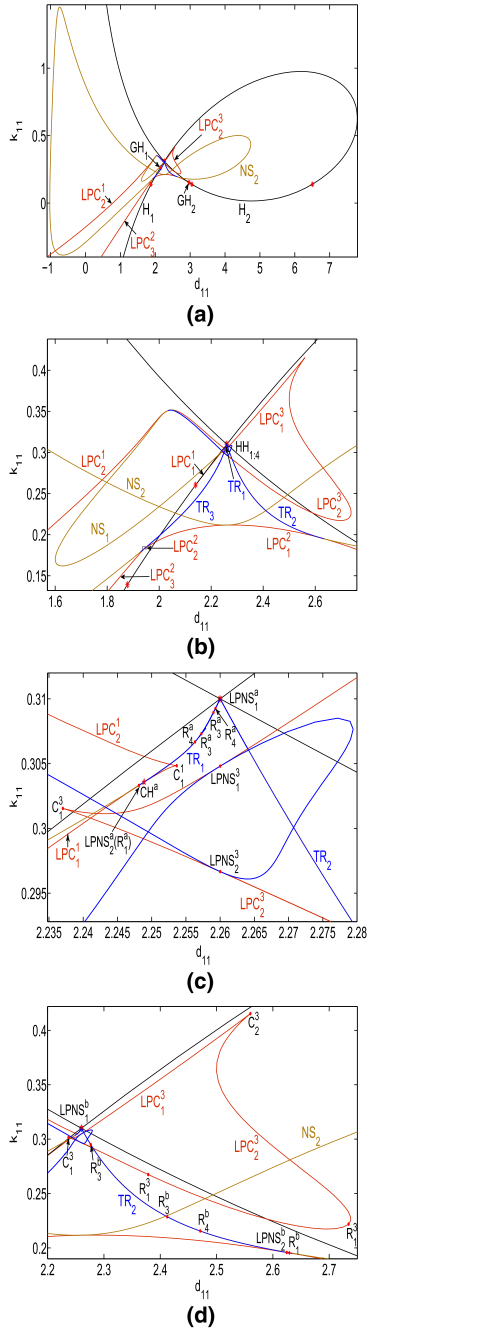

Fig. 14 **a** Bifurcation diagram for $k_{22} = 1.01$ near the 1:4 resonant Hopf–Hopf bifurcation. **b** Expanded view close to the singularity point $HH_{1:4}$ for $(d_{11}^*, k_{11}^*) = (2.260000, 0.310000)$. **c** Bifurcation diagram associated with the Neimark–Sacker bifurcation curve TR_1. **d** Bifurcation diagram related to the Neimark–Sacker bifurcation curve TR_2. **e** Bifurcation diagram with respect to the Neimark–Sacker bifurcation curve TR_3. **f** Schematic diagram in the vicinity of the curves $LPC^2_{1,2,3}$

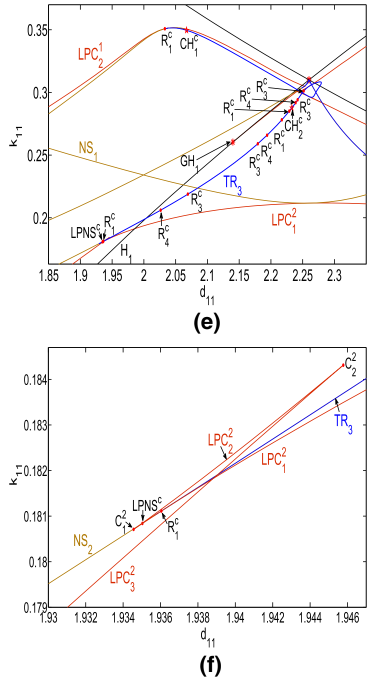

Fig. 14 continued

Sacker points $LPNS^a_{1,2}$ emerge at the ends of this branch. Moreover, a 1:1 resonance point R^a_1 is encountered on both the curves TR_1 and LPC^1_1.

On the branch TR_2 (Fig. 14d), there also exist a couple of Fold-Neimark–Sacker points $LPNS^b_{1,2}$, one of which $LPNS^b_1$ is near to $HH_{1:4}$, and the other $LPNS^b_2$ is close to R^b_1 . Four strong resonances such as a 1:1, two 1:3 and a 1:4 resonance points appear, which are denoted as R^b_1, R^b_3 and R^b_4, respectively. In addition, this branch ends with R^b_1.

On the branch TR_3 (Fig. 14e), the difference from $TR_{1,2}$ is that it forms a closed loop. The most notable is that a couple of Chenciner bifurcation points $CH^c_{1,2}$ emerge here, one CH^c_1 is close to LPC^2_1, and the other CH^c_2 is between R^c_1 and R^c_4. In the left half of CH^c_1, a 1:1 resonance point R^c_1 divides this curve into TR_3 and NS_1. In the left half of CH^c_2, there exist three 1:1 resonance points R^c_1 and a Fold-Neimark–Sacker point $LPNS^c$, among them, $LPNS^c$ divides this curve into TR_3 and NS_2 (see Fig. 14f). Moreover, there are two 1:3 and two 1:4 resonance points, denoted as R^c_3 and R^c_4, respectively. In the right half of CH^c_2, the branch produces a couple of 1:3 resonance points R^c_3 and a 1:4 resonance point R^c_4. Furthermore, the left part of $CH^c_{1,2}$ with positive index $c(0)$ are the subcritical Neimark–Sacker

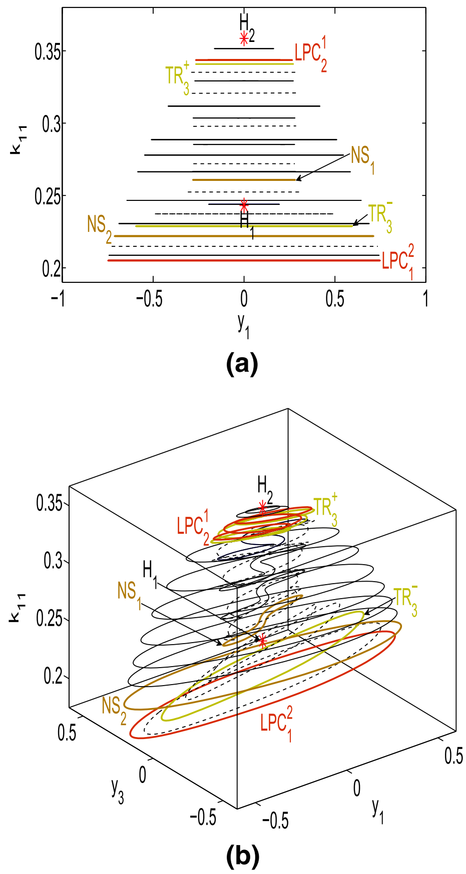

Fig. 15 **a** Cyclic bifurcation structure for $d_{11} = 2.1$ and $k_{22} = 1.01$ on 2D plane. **b** Cyclic bifurcation structure in 3D space with respect to the labels in **a**

bifurcations, which shows the presence of unstable torus, whereas the part between $CH^c_{1,2}$ with negative index $c(0)$ is the supercritical Neimark–Sacker bifurcation, which gives birth to stable torus.

In Fig. 15, more complex cyclic bifurcation behaviors occur when the same d_{11} is fixed. The negative index $FLC = -0.007540120$ indicates that the Hopf bifurcation point H_1 develops a family of stable limit cycles, then a cyclic neutral saddle NS_1 arises at $k_{11} = 0.2607852$. A cyclic limit point LPC^1_2 is detected as k_{11} increases, the stability of the limit cycles remains unchanged due to the index $c(0) = -14.07494$. Two cyclic Neimark–Sacker bifurcation points are detected at TR^+_3: $k_{11} = 0.3426828$ with $c(0) = 0.285738$, and TR^-_3: $k_{11} = 0.2287775$ with $c(0) = 0.0002770011$, which indicate that the limit cycles born at $TR^{\pm}_3$ are both unstable, thus two unstable torus can be observed. So far the limit cycles have become distorted with complex resonance. The stability of the limit cycles restores via LPC^2_1 with $c(0) = -0.09781862$, then a cyclic neutral saddle NS_2 emerges at $k_{11} = 0.2219031$. Finally, the limit cycles begin a recurrence after reaching the point H_2 with $FLC = -0.05429647$.

A more complex loop between two Hopf bifurcation points $H_{1,2}$ can be shown as: $H_1 \xrightarrow{SC} NS_1 \xrightarrow{SC} LPC^1_2 \xrightarrow{SC} TR^+_3 \xrightarrow{UC} TR^-_3 \xrightarrow{UC} LPC^2_1 \xrightarrow{SC} NS_2 \xrightarrow{SC} H_2 \xrightarrow{SC} NS_2 \xrightarrow{SC} LPC^2_1 \xrightarrow{UC} TR^-_3 \xrightarrow{UC} TR^+_3 \xrightarrow{SC} LPC^1_2 \xrightarrow{SC} NS_1 \xrightarrow{SC} H_1$. Within the region of LPC^1_2 and TR^+_3, the stable limit cycles arisen from the wheelset coexist. Within the region of TR^+_3 and TR^-_3, the stable limit cycles arisen at H_1 and LPC^2_1 coexist with the unstable limit cycles born at TR^+_3, which indicates the presence of an unstable torus via TR^+_3. Within the region of TR^-_3 and LPC^2_1, the stable limit cycles arisen at LPC^2_1 coexist with the unstable limit cycles born at TR^-_3, which indicates the presence of another unstable torus via TR^-_3.

5 Conclusions

Due to the interaction of lateral and yaw motion of the simplified railway wheelset, the dynamics of the non-resonant and near-resonant Hopf–Hopf bifurcations are taken into account in this paper, which involves local and global dynamical scenarios, respectively. The parameter k_{22} plays a crucial role in the transitions of distinct Hopf–Hopf bifurcations, and the result shows that the ratio of the oscillation frequencies ω_1/ω_2 at the Hopf–Hopf singularity point will reduce with the decrease in k_{22} within a certain range.

At first, the local dynamics with respect to the truncated normal form of the non-resonant Hopf–Hopf bifurcation on this wheelset model has been presented, which belongs to the "difficult" case VI. Two Neimark–Sacker branches $TR_{1,2}$ without emerging strong resonance indicate that the running wheelset will not produce the maximum oscillation amplitude induced by the resonance point. The wheelset gives birth to an unstable 2D torus when undergoing TR_1, and a stable 2D torus is created at TR_2. In addition, the unstable 2D torus will lead to a stable 3D torus after suffering a heteroclinic bifurcation.

Secondly, the global dynamics of five near-resonant Hopf–Hopf bifurcations have been discussed. These results show that near-resonant Hopf–Hopf bifurcation scenario becomes more complicated as k_{22} decreases. In particular, an extremely complex global bifurcation phenomenon occurs when k_{22} is reduced to satisfy the case close to 1:4 resonance, which is the most remarkable condition that affects wheelset hunting motions and resonances, as follows:

(1) Case I: near the 1:1 resonant Hopf–Hopf bifurcation. The intersection of two Hopf curves $H_{1,2}$ does not produce a closed loop, a neutral saddle curve NS between $H_{1,2}$ forms a closed curve starting and ending at the singularity point $HH_{1:1}$. Two generalized Hopf bifurcation points $GH_{1,2}$ are connected by the cyclic fold curve LPC, and the cyclic cusp point C emerging on LPC is near to GH_1.
(2) Case II: near the 2:3 resonant Hopf–Hopf bifurcation. The curves $LPC_{1,2}$ born at $GH_{1,2}$ intersect at a cusp point C. Two Neimark–Sacker branches $TR_{1,2}$ born at $HH_{2:3}$ are connected by a neutral saddle curve NS, which give birth to a closed curve after two turns. A Chenciner bifurcation point CH^b emerges on TR_2, and several strong resonance points are detected on $TR_{1,2}$.
(3) Case III: near the 1:2 resonant Hopf–Hopf bifurcation. This case undergoes the similar bifurcation as near the 2:3 resonant condition, for example, the curves $LPC_{1,2}$ in both cases intersect at a cusp point C, and a Chenciner bifurcation point CH^b is detected on TR_2. The discrepancy is that the number of the strong resonance points on $TR_{1,2}$ grows.
(4) Case IV: near the 1:3 resonant Hopf–Hopf bifurcation. Compared with the Hopf–Hopf bifurcation near 2:3 and 1:2 resonance, the similar scenario is that a neutral saddle curve NS joins two Neimark–Sacker branches $TR_{1,2}$ and forms a closed curve after two turns, the discrepancy is that the number and structure of cyclic fold curves have changed. The cyclic fold curves born at $GH_{1,2}$ no longer encounter at a cusp point, the curve LPC_1^1 born at GH_1 forms C^1 and then joins LPC_2^1. The curve LPC_1^2 born at GH_2 forms C_1^2 with LPC_2^2, then the curve LPC_2^2 ends at C_2^2 along with LPC_3^2. In particular, a couple of points $CH^{a,b}$ emerge on $TR_{1,2}$, respectively. More strong resonance points can be detected on $TR_{1,2}$.
(5) Case V: near the 1:4 resonant Hopf–Hopf bifurcation. Compared with the previous conditions near resonance, it is the most complicated one that contains quite rich dynamics scenario. One neutral saddle curve NS_1 joins $TR_{2,3}$ and the other NS_2 joins $TR_{1,3}$, which form a closed curve after four turns. The curves $LPC_{1,2}^1$ and $LPC_{1,2,3}^2$ born at $GH_{1,2}$ are analogous in structure and quantity to the 1:3 resonant case. A particular structure is that the presence of $LPC_{1,2}^3$ and TR_3. A couple of Chenciner bifurcation points $CH_{1,2}^c$ divide TR_3 into three parts, the branch TR_3 between $CH_{1,2}^c$ with negative index $c(0)$ shows the existence of stable torus, and the positive index $c(0)$ of other parts of this branch indicates the presence of unstable torus. In addition, the significant increase in the number of the strong resonance points on $TR_{1,2,3}$ means that more complex resonance phenomena occur.

At last, under the near-resonant conditions, the parameter d_{11} is fixed at 2.1 to observe the cyclic bifurcation structures when k_{11} changes. These results show the coexistence of multiple limit cycles arisen from the wheelset. The loop of equilibria and limit cycles detected between two Hopf bifurcation points $H_{1,2}$ indicates that the wheelset will develop a cyclical motion in lateral and yaw direction, as follows:

- For case I: $H_1 \xrightarrow{SC} NS^- \xrightarrow{SC} NS^+ \xrightarrow{SC} H_2 \xrightarrow{SC} NS^+ \xrightarrow{SC} NS^- \xrightarrow{SC} H_1$, which indicates that the stable limit cycles emanated from the wheelset at $H_{1,2}$ coexist.
- For case II: $H_1 \xrightarrow{SC} LPC_1 \xrightarrow{SC} TR_1 \xrightarrow{UC} LPC_2 \xrightarrow{SC} NS \xrightarrow{SC} H_2 \xrightarrow{SC} NS \xrightarrow{SC} LPC_2 \xrightarrow{UC} TR_1 \xrightarrow{SC} LPC_1 \xrightarrow{SC} H_1$, which indicates that the coexistence of stable limit cycles arisen from the wheelset within the region of LPC_1 and TR_1. Within the region of TR_1 and LPC_2, the stable limit cycles born at LPC_2 coexist with an unstable torus via TR_1.
- For case III: $H_1 \xrightarrow{SC} LPC_1 \xrightarrow{SC} TR_1 \xrightarrow{UC} LPC_2 \xrightarrow{SC} NS \xrightarrow{SC} H_2 \xrightarrow{SC} NS \xrightarrow{SC} LPC_2 \xrightarrow{UC} TR_1 \xrightarrow{SC} LPC_1 \xrightarrow{SC} H_1$, which indicates that the cyclic bifurcation structure is similar to case II.
- For case IV: $H_1 \xrightarrow{SC} LPC_2^1 \xrightarrow{SC} TR_1 \xrightarrow{UC} LPC_1^2 \xrightarrow{SC} NS \xrightarrow{SC} H_2 \xrightarrow{SC} NS \xrightarrow{SC} LPC_1^2 \xrightarrow{UC} TR_1 \xrightarrow{SC} LPC_2^1 \xrightarrow{SC} H_1$, which indicates that the stable limit cycles emanated from the wheelset coexist within the region of LPC_2^1 and TR_1. Within the region of TR_1 and LPC_1^2, the stable limit cycles born at LPC_1^2 coexist with an unstable torus via TR_1.
- For case V: $H_1 \xrightarrow{SC} NS_1 \xrightarrow{SC} LPC_2^1 \xrightarrow{SC} TR_3^+ \xrightarrow{UC} TR_3^- \xrightarrow{UC} LPC_1^2 \xrightarrow{SC} NS_2 \xrightarrow{SC} H_2 \xrightarrow{SC} NS_2 \xrightarrow{SC}$

$LPC_1^2 \xrightarrow{UC} TR_3^- \xrightarrow{UC} TR_3^+ \xrightarrow{SC} LPC_2^1 \xrightarrow{SC} NS_1 \xrightarrow{SC} H_1$, which indicates that the coexistence of stable limit cycles arisen from the wheelset within the region of LPC_2^1 and TR_3^+. Within the region of TR_3^+ and TR_3^-, the stable limit cycles born at H_1 and LPC_1^2 coexist with an unstable torus via TR_3^+. Within the region of TR_3^- and LPC_1^2, the stable limit cycles born at LPC_1^2 coexist with another unstable torus via TR_3^-.

These obtained results indicate that the change in frequency ratio induced by the intersection of the lateral and yaw motion of the unbalanced wheelset will greatly affect the hunting motions and resonances of railway vehicles. Therefore, appropriately increasing the value of k_{22} is helpful to maintain the vehicle stability. It is noted that what we present in this paper is only the global dynamics scenarios of the non-resonant and the near-resonance Hopf–Hopf bifurcations in a simplified wheelset model, while it will be an extremely complex task when it comes to discuss a bogie frame or even a carbody. These issues are for future research to investigate.

Acknowledgements This work is supported by the Fundamental Research Funds for the Central Universities under Project No. 2021QY005, the State Key Laboratory of Traction Power, Southwest Jiaotong University under Project No. TPL2001, the National Natural Science Foundation of China (Grant Number 51905454), and Independent R&D Project of the State Key Laboratory of Traction Power (Grant Number 2019TPL_T22).

Data availability We declare that the datasets analyzed during the current study are available in the following public domain resources: [9,10].

Declaration

Conflict of interest The authors declare that they have no conflict of interest.

References

1. Kuznetsov, Y.A.: Elements of Applied Bifurcation Theory, 3rd edn. Springer, New York (2004)
2. Wiggins, S.: Introduction to Applied Nonlinear Dynamical Systems and Chaos. Springer, Berlin (1990)
3. Dong, H., Zeng, J., Xie, J.H., et al.: Bifurcation\instability forms of high speed railway vehicles. Sci. China Technol. Sci. **56**(7), 1685–1696 (2013)
4. Huang, C.H., Zeng, J., Liang, S.L.: Influence of system parameters on the stability limit of the undisturbed motion of a motor bogie. Proc. Inst. Mech. Eng. Part F J. Rail Rapid Transit. **228**(5), 522–534 (2014)
5. Huang, C.H., Zeng, J.: Suppression of the flexible carbody resonance due to bogie instability by using a DVA suspended on the bogie frame. Veh. Syst. Dyn. (2021). https://doi.org/10.1080/00423114.2021.1930071
6. Revel, G., Alonso, D.M., Moiola, J.L.: Numerical semi-global analysis of a 1:2 resonant Hopf–Hopf bifurcation. Physica D **247**, 40–53 (2013)
7. Revel, G., Alonso, D.M., Moiola, J.L.: Interactions between oscillatory modes near a 2:3 resonant Hopf-Hopf bifurcation. Chaos **20**, 043106 (2010)
8. Revel, G., Alonso, D.M., Moiola, J.L.: A gallery of oscillations in a resonant electric circuit: Hopf–Hopf and fold-flip interactions. Int. J. Bifurc. Chaos Appl. Sci. Eng. **18**, 481 (2008)
9. Yabuno, H., Okamoto, T., Aoshima, N.: Stabilization control for the hunting motion of a railway wheelset. Veh. Syst. Dyn. **35**, 41–55 (2001)
10. Yabuno, H., Okamoto, T., Aoshima, N.: Effect of lateral linear stiffness on nonlinear characteristics of hunting motion of a railway wheelset. Meccanica **37**(6), 555–568 (2002)
11. Ge, P., Wei, X., Liu, J., et al.: Bifurcation of a modified railway wheelset model with nonlinear equivalent conicity and wheelCrail force. Nonlinear Dyn. **102**(1), 79–100 (2020)
12. Cheng, L.F., Wei, X.K., Cao, H.J.: Two-parameter bifurcation analysis of limit cycles of a simplified railway wheelset model. Nonlinear Dyn. **93**, 2415–2431 (2018)
13. True, H.: Dynamics of a rolling wheelset. Appl. Mech. Rev. **46**, 438–444 (1993)
14. Wickens, A.H.: The dynamics stability of a simplified four-wheel railway vehicle having profiled wheels. Int. J. Solids Struct. **1**, 385–406 (1965)
15. Xu, G., Troger, H., Steindl, A.: Global analysis of the loss of stability of a special railway body. In: Schiehlen, W. (ed.) Nonlinear Dynamics in Engineering Systems, pp. 345–352. Springer, Berlin (1990)
16. Wen, G.L., Xu, H.D., Xie, J.H.: Controlling Hopf–Hopf interaction bifurcations of a two-degree-of-freedom self-excited system with dry friction. Nonlinear Dyn. **64**, 49–57 (2011)
17. Parks, P.C.: A new proof of Hermite's stability criterion and a generalization of Orlando's formula. Int. J. Control **26**(2), 197–206 (1977)
18. Chow, S., Li, C., Wang, D.: Normal Forms and Bifurcation of Planar Vector Fields. Cambridge University Press, Cambridge (1994)
19. Dhooge, A., Govaerts, W., Kuznetsov, Y.A.: MATCONT: a MATLAB package for numerical bifurcation analysis of ODEs. ACM Trans. Math. Softw. **37**(9), 141–164 (2003)
20. Balanov, A.G., Janson, N.B., Schöll, E.: Delayed feedback control of chaos: bifurcation analysis. Phys. Rev. E **71**, 016222-1, 9 (2005)